Smart Materials and Structures

PAPER

Optimal turbine blade design enabled by auxetic honeycomb

To cite this article: Aniket Pal *et al* 2020 *Smart Mater. Struct.* **29** 125004

Smart Mater. Struct. **29** (2020) 125004 (12pp)

https://doi.org/10.1088/1361-665X/abbd1d

Optimal turbine blade design enabled by auxetic honeycomb

Aniket Pal[1,2], Katia Bertoldi[1,3], Minh Quan Pham[4], Megan Schaenzer[4] and Andrew J Gross[1,5]

[1] Harvard John A. Paulson School of Engineering and Applied Sciences, Harvard University, 29 Oxford Street, Cambridge, MA 02138, United States of America
[2] School of Industrial Engineering, Purdue University, 315 N. Grant Street, West Lafayette, IN 47907, United States of America
[3] Kavli Institute, Harvard University, Cambridge, MA 02138, United States of America
[4] Siemens Energy Canada Limited, 9505 Cote de Liesse Road, Montreal QC H9P 1A5, Canada
[5] Department of Mechanical Engineering, University of South Carolina, 541 Main Street, Columbia, SC 29208, United States of America

E-mail: andrewgross@sc.edu

Received 21 July 2020, revised 2 September 2020
Accepted for publication 30 September 2020
Published 26 October 2020

Abstract

Gas turbine blades are subjected to unusually harsh operating conditions—rotating at high velocities in gas streams whose temperature can exceed the melting temperature of the blade. In order to survive these conditions, the blade must efficiently transfer heat to an internal cooling flow while effectively managing mechanical stresses. This work describes a new design strategy for the internal structure of turbine blades that makes use of architected materials tailored to reduce stresses and temperatures throughout the blade. A full 3D characterization was first performed to determine the thermomechanical properties of generalized honeycomb materials with different design parameters: honeycomb angle and wall thickness. A turbine blade cross section was then divided into multiple discrete domains so that different generalized honeycomb materials could be assigned to each of the domains. Optimization of the material assignments was performed in order to minimize the stress ratio—ratio of the maximum Mises' stress and the temperature dependent yield stress—in the entire model. The optimized design showed substantial improvement with respect to a baseline model; the factor of safety was increased by 171%, while the maximum Mises' stress and temperature decreased by 42% and 72% respectively. The use of generalized honeycomb materials allows for local control of the material properties to tune the performance of the turbine blade. The results of the optimization clearly indicate that auxetic honeycombs outperform conventional designs; since their lower in-plane stiffness helps to reduce stresses caused by thermal gradients. Our results demonstrated the feasibility of using 3D-printing compatible architected materials in turbine blades to increase their factor of safety and potentially increase operating temperatures to improve thermal efficiency.

Supplementary material for this article is available online

Keywords: architected materials, lattice materials, honeycomb, auxetic, optimization, CMA-ES, turbine blade, structural analysis, thermal analysis, evolutionary strategy

(Some figures may appear in colour only in the online journal)

1. Introduction

Gas turbines are one of the most versatile and commonly used prime movers in the world. They are used in a variety of applications like turbofan engines, turboprop engines, and gas power plants. Continuous increase in energy demand combined with the need to reduce harmful emissions from fossil fuel based power generation has created intense interest to increase the efficiency of gas turbines. Raising the gas temperature at the turbine inlet is one of the most effective avenues to improve the thermal efficiency of gas turbines, however, this approach is limited by the maximum allowable temperature of the turbine blade material [1]. Convective cooling—passing of cold air through internal passages of the blade body to reduce temperature—is commonly utilized in high pressure turbine blades. As a result, the blades can operate in an extraordinarily harsh environment with high temperature and pressure. Environmental effects alone cause substantial stresses in these turbine blades, with regions of high stress concentration that are difficult to eliminate and eventually lead to their failure [2]. Even optimized designs often lead to non-uniform cooling with large, stress-producing temperature gradients across the turbine blade [3–5].

Gas turbine blades also rotate at very high speeds (>3600 RPM), which produces mechanical loading from large centrifugal forces (figures 1(a), (b)). The airfoil cross-section of the blade, non-homogeneous distribution of cooling channels, and position of the shroud at the tip of the blade are necessary for good aerodynamic performance, however, these elements create a non-uniform stress profile (figure 1(c)) on the turbine blade [6, 7]. Furthermore, the thermal stress due to uneven temperature distribution (figure 1(d)) along the blade exacerbates the stress profile [8, 9]. Thus, the hot gas temperature is restricted by only a small portion of the turbine blade, which reaches the maximum allowable temperature and stress levels, while the rest of the blade operates below those levels. It would be desirable to have a turbine blade design which generates lower and more uniform thermal and mechanical stress fields while maximizing the cooling of the blade in order to improve the efficiency of gas turbines.

The capability to vary the thermomechanical behavior and density of a material throughout a turbine blade would enable a design that minimizes the peak stress generated during its operation. Such functionally graded properties can be obtained by using architected cellular materials, where freedom in specifying material properties comes from the ability to modify the local cellular architecture [10–14]. Additionally, ordered cellular architectures can efficiently transfer the properties of bulk materials to lower densities materials while harnessing beneficial aspects of material anisotropy [15–19]. Moreover, the porosity of cellular architected materials uniquely benefit turbine blade design in two ways: *(i)* the porous structure also serves as an efficient heat exchanger to improve convective cooling between the blade and the cooling air; *(ii)* a gradual variation in relative density, from fully solid towards void, can be achieved in the porous material to decrease steep stress and temperature gradients.

Topology optimization has been a popular method to design mechanically efficient cellular materials. Cheng *et al* used topology optimization of graded lattice structures (beam-based open-cell structures) subject to stress constraints to achieve predictable yield performance of static structures [20]. Using relative density as the only design variable, the authors computed the effective elastic properties of the lattice material, which was used to minimize the weight of the structure under stress constraints. Wang *et al* used similar graded lattices, but with the individual unit cells (mesostructures) themselves being graded to ensure good connectivity and reduce stress concentration between adjacent mesostrcutures [21]. A slightly different approach was employed by Zhang *et al*, who increased the controllable design variables by including different microstructures which could be assigned to prespecified domains in the structure [22]. This two-tier optimization, of both the shape and the domain-based microstructure, helped improve the structural stiffness over simply graded lattices. Das *et al* demonstrated a multiphysics (thermo-mechanical) topology optimization to enhance structural performance while improving heat dissipation at the same time [23]. Instead of using lattices (ordered architecture), porous cells (random architecture) were used in this approach, with pore size and relative density being the design variables. Contrastingly, a graded lattice-based approach was employed by Takezawa *et al* to improve fluid flow based convective heat transfer, without considering mechanical responses [24].

Successful applications of topology optimization include the creation of bio-scaffolds for hip implants [25, 26], the design of aerospace structures [27], and elucidating the structure–property relationship in plants [28]. In the field of turbomachinery, however, most topology optimization research have focused on improving the contour of the blades [29, 30]. Some recent research have tried to improve the material layout or reduce the mass of turbine blades, but have failed to consider the thermal aspects altogether [31] or have reached results with unwanted thermal stress concentrations [32].

Here we present a materials-by-design approach applied to a turbine blade using architected cellular materials with high structural efficiency. The architected materials use a repeating pattern of 2.5D, honeycomb shaped unit cells, and allow for the modification of material characteristics locally by controlling the geometric parameters of the cells. Optimal local material properties in the blade are found by creating a database of material properties and then finding the optimal assignment of these materials throughout the blade structure. This approach is motivated by the use of material domains in [22], but selects parameter optimization over topology optimization for ease of implementation in this thermomechanical problem with temperature dependent material properties. The high degree of local control enables our optimized turbine blade to achieve more favorable temperature and stress profiles than existing designs. Taking into cognizance the loading characteristics of a turbine blade, we use an orthotropic, 2.5D design: 2D honeycomb materials extruded along the radial direction of rotation for the turbine blade. The direct load path of the extrusion provides high strength to withstand the centrifugal force,

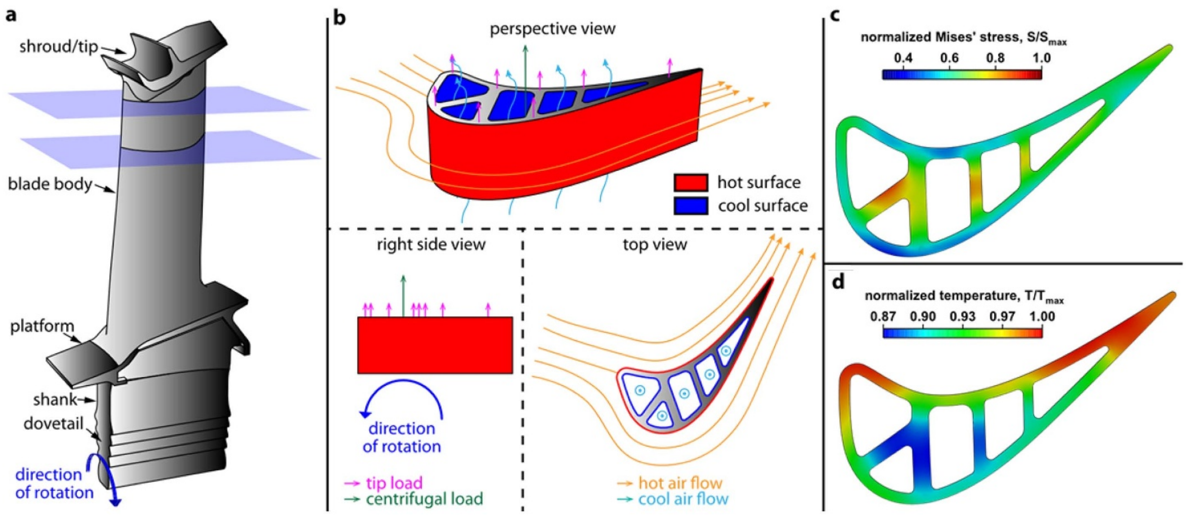

Figure 1. Design and performance of a traditional turbine blade. (a) Image of a turbine blade showing its different parts and the direction of rotation. The two sectional planes indicate the section used for all analysis. (b) Orthogonal and perspective view of the section showing the mechanical and thermal loads acting on it. (c), (d) Top view showing the results from a finite element (FE) analysis of the (c) stress and (d) temperature fields generated in the turbine blade section due the mechanical and thermal loads acting on it (shown in panel B).

which is the dominant mechanical load on the turbine blade [6]. The 2D cellular structure on the orthogonal plane provides the ability to tune the mechanical and thermal properties (relative density, effective in-plane elastic moduli, effective in-plane thermal conductivities, etc.) in order to optimize the design. We set up an evolutionary strategy (ES) based optimization to minimize a measure of peak stress in the model, subject to multiple constraints. The cellular architecture of the new blade is enabled by recent advances in additive manufacturing with metallic materials [33–35].

We structure our manuscript as follows: in the Methods section a parametric study is conducted over the primary design parameters of the unit cell to characterize its range of mechanical and thermal properties. We then create subdomains in the turbine blade cross-section over which we assign uniform unit cell parameters and therefore homogeneous effective material properties. Finally, we set up an optimization process using the covariance matrix adaptation evolution strategy (CMA-ES) algorithm [36] to determine the optimum material assignments for each of the subdomains, subject to local and global constraints. In the Results section we discuss the optimized design and show the improvements over the baseline design, followed by concluding remarks regarding future work.

2. Geometry

In this study we focus on a generalized honeycomb material defined by the two lattice vectors $\mathbf{a}_1 = [0, 2l\sin\theta]$ and $\mathbf{a}_2 = [l(1\text{-}\cos\theta), l\sin\theta]$, where l is the length of the edges and θ is the internal angle between the horizontal and inclined edges of the honeycombs (see figure 2(a)). The relative density $\bar{\rho}$ is controlled by the thickness ratio t/l, where t is the wall thickness. Note that, to avoid stress concentrations we modified all corners to have a fillet with radius equal to the wall thickness t. By varying the angle θ and thickness ratio t/l (figure 2(c)), we achieve a broad range of relative densities (4.5% to 63.5%, figure 2(e)); where the relative density $\bar{\rho}$ is calculated as the ratio between the solid volume of the generalized honeycomb and the volume of the unit cell described by the periodicity vectors. The range of angles for θ is restricted between 60° and 180° due to the geometry of a hexagon; for beam t/l ratio, we chose a range of 0.04 to 0.52 to produce geometrically allowable designs that can be 3D printed with commercially available metal 3D printers at the appropriate length scale for the turbine blade selected for this study. The domain space of feasible parameter combinations (green) is shown in figure 2(d), as the thickness of the beams and the fillet radii between them get larger, many parameter combinations becoming infeasible (orange and red) restricting designs to a narrower range of angles for θ.

3. Numerical characterization of the mechanical and thermal properties of a generalized honeycomb material

The mechanical properties of metamaterial structures with honeycomb designs have been of interest to researchers for many decades [37–44]. These studies have focused on 2D honeycombs [37, 41, 44] have not included auxetic geometries [41, 42], do not provide complete anisotropic elastic characterization [37, 40, 42, 43], or do not consider multiple cell parameters [41, 42, 44]. Due to our need for 3D anisotropic elastic characterization on a broad set of extruded honeycombs across diverse geometric variations we have performed our own characterization. This additional characterization is further motivated by our need for the thermal properties of generalized honeycomb materials, which have not attracted similar attention and have not been characterized over the wide-ranging set of geometries considered here.

To characterize both the mechanical and thermal properties of the architected materials, we performed FE simulations

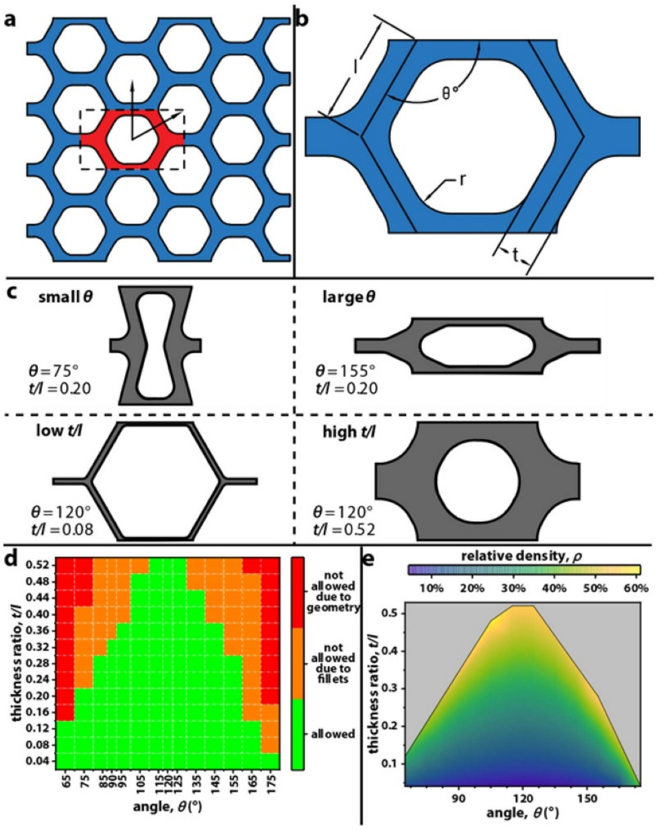

Figure 2. Generalized honeycomb unit cell: parameterization and geometric properties. (a) A 2D tessellation of hexagonal cells showing the selected rectangular unit cell and the lattice vectors. (b) Characteristic design parameters of the unit cell: length l, wall thickness t, angle θ, and fillet radius r. (c) Effect of unit cell parameters θ and t/l on the shape of the generalized honeycomb material. (d) Design space showing which combination of parameters lead to feasible (green) and infeasible (orange and red) designs. (e) Variation of relative density $\bar{\rho}$ (ratio of solid volume to unit cell volume) with θ and t/l.

of the 3D extruded unit cells with periodic boundary conditions using the commercial software Abaqus 2017 (SIMULIA™, Dassault Systèmes®). All FE simulations were performed by generating a hexahedral mesh comprising of quadratic elements with reduced integration (Abaqus element type: C3D20R). We varied our mesh density with the thickness of the beams in order to achieve accurate results. We performed a mesh convergence study (figure S1 (available online at https://stacks.iop.org/SMS/29/125004/mmedia)) and found that reducing the element size smaller than $t/6$ did not change the simulation results, and the results showed no dependence on the number of elements used in the direction of extrusion due to the presence of periodic boundary conditions.

3.1. Mechanical properties

We started by focusing on the mechanical properties and conducted static analyses in which we subjected the unit cell to nine different strain states (uniaxial, biaxial, and shear aligned with each of the three planes of symmetry) to allow for calculation of the orthotropic elastic stiffness tensor. In each prescribed strain state, the average deformation and strain energy stored in the unit cell are related to the average stress in the unit cell according to the Hill-Mandel principle [45] The relationship between the average stresses and average strains permits calculation of the nine independent elastic constants [46].

Since the constitutive behavior of the bulk material was modeled as an isotropic, linearly elastic solid, the elastic modulus of the bulk material used in the simulations can be simply scaled to apply the results of these simulations to generalized honeycomb materials constructed with bulk materials of any stiffness. It is noted here that no simple method or scaling can be performed to transfer the results to materials with different Poisson's ratio. Importantly, nickel-chromium based super-alloys, which are used to fabricate most turbine blades (due to its high temperature capability and oxidation resistance) exhibits a temperature dependent Poisson's ratio. To capture this effect, we performed the simulations twice; once with the Poisson's ratio at room temperature and again with the Poisson's ratio at the maximum operating temperature. The influence of the Poisson's ratio of the bulk material on the elastic properties of the generalized honeycomb was then assumed to vary linearly between these two extremes, while the effective stiffness of the generalized honeycomb was simply scaled according to the temperature dependent elastic modulus of the bulk material. In this way, the stiffness matrix for the generalized honeycomb incorporates the temperature dependent elastic modulus and Poisson's ratio of the bulk material.

The characterization of the mechanical properties—relative elastic moduli and Poisson's ratio—is shown in figure 3, which cover large ranges within our design space. This data is also provided in tabular format in table S1. Using the strain energy calculated from the FE simulations we constructed the full orthotropic stiffness matrix, and consequently calculated the elastic moduli and Poisson's ratios for each unit cell design. As anticipated, all elastic moduli have a strong correlation with the relative density (figures 2(d), S2): designs with higher t/l values are stiffer. E_{33} depends only on the relative density $\bar{\rho}$ of the honeycomb since the lattice structure is extruded along the *3* direction. Quantitatively, the specific stiffness $E_{33}/\bar{\rho}$ is found to be constant and identical to that of the bulk material. The in-plane elastic modulus E_{22} increases around $\theta = 90°$; as the hexagons degenerate into rectangles and have struts aligned in the *2* direction. The generalized honeycomb produces reentrant geometry for angle $\theta < 90°$, which leads to negative values for the in-plane Poisson ratios ν_{12} and ν_{21}. (figure 3) for most thickness ratios t/l. For dense designs with $t/l \geq 0.24$, the smallest permissible value for the angle θ increases, and no designs in this range of thickness ratio t/l are found to be auxetic. Even reentrant designs with $\theta = 85°$ are found to be non-auxetic when $t/l \geq 0.24$. Auxetic designs can always be found for $t/l \leq 0.2$. The out-of-plane Poisson's ratios ν_{31}, and ν_{32} have no dependence on the geometric parameters of the unit cell due to the extruded design. Overall, results from the parametric study are consistent with that found in prior investigations [37–44, 47–50], while providing the complete database of mechanical properties needed for subsequent optimization of the turbine blade.

3.2. Thermal properties

Next, we performed heat transfer FE simulations on the unit cells to calculate the thermal conductivity and the maximum possible amount of heat that can be transferred from the solid region of the unit cells to the surrounding cooling flow. We find that the relative thermal conductivities show a high correlation with the relative density $\bar{\rho}$, where the thicker beams allow faster transport of heat. Due to the extruded nature of the designs, k_{33} behaves similar to E_{33}, depending only on $\bar{\rho}$, with $k_{33}/\bar{\rho}$ of all the cellular materials being identical to that of the bulk material. The maximum heat these structures are able to flux to the surrounding cooling flow however decreases with relative density $\bar{\rho}$. Thinner beams, especially with extreme angles have higher surface area to volume ratio, and are therefore capable of high convective heat transport.

4. Optimization

Once the mechanical and thermal properties of the generalized honeycomb material have been characterized, they can be utilized to assign customized local properties to the turbine blade. This approach allows us to move away from the traditional design of a solid cross-section with hollow passages for air flow (figure 5(a)) to a design that avoids large gradients by making use of graded porosity. We chose to apply the architected design to only the body of the turbine blade (identified in figure 1(a)), as this part of the blade has the most complex cooling channels inside and has the most interaction with the hot fluid flow. We perform our optimization on an extruded 2D section from the top of the blade body to demonstrate the effectiveness of our design while keeping the optimization process computationally feasible. Once demonstrated in 2.5D, the approach can easily be applied throughout the blade body to determine the assignments of architected materials in the optimal design of an entire 3D turbine blade.

Optimizing the parameters of each unit cell in the blade cross-section, however, is computationally prohibitive; so, we divided up the blade cross-section into 23 discrete domains (figure 5(b)), each of which is to be homogeneously assigned a generalized honeycomb material from our database. The domains are arranged in a layered structure containing 11, 7, 4 and 1 domains from the outermost to the innermost layer. We kept an outer layer of solid Inconel to maintain the airfoil shape free of disturbance from the architected materials assigned these domains. This layer was again divided into four more sub-layers, allowing them to be assigned as either solid or architected, thus allowing the thickness of this solid layer to be a design parameter. If assigned as architected, the sub-layer would take on the properties of the nearest domain in the interior of the blade. The domains assigned a generalized honeycomb material are parameterized by the four variables shown in figure 5(c). Each unique combination of these parameters specifies the design of the generalized honeycomb (θ and $\bar{\rho}$), its orientation with respect to the blade geometry (α), and the temperature of the cooling air flowing through it (represented with by the heat flux fraction φ). Note that, since from the results of our FE simulations we observed that most of the properties were very strongly correlated with the relative density $\bar{\rho}$ of the design (figure S2), we chose to use relative density $\bar{\rho}$ instead of wall thickness ratio t/l as a defining parameter of the unit cell for the optimization process. Furthermore, we reshaped our domain space to have a rectangular shape in order to remove conditional parameter selection during the optimization process and hence make it simpler. An example of this transformation (using elastic modulus E_{11}) is shown in figures 5(d)–(f).

Each turbine blade design was simulated with the thermomechanical loading of normal operating conditions. Simulations were performed in Abaqus 2017 on a model with 15 600 quadratic hexahedral elements with reduced integration (C3D20R). First, a heat transfer simulation was performed, where convective heating is assumed for the interaction between the hot fluid and the turbine blade. Heat transfer to the cooling air was modeled with the Abaqus user subroutine (DFLUX), which directly defined the heat flux per unit volume (as set by the optimization algorithm and limited by the properties of the selected generalized honeycomb) for each domain. Once the thermal simulation was complete, the results were used as initial conditions to calculate the stress caused by thermal expansion in a mechanical simulation. This simulation directly included centrifugal body forces present in the simulated region of the turbine blade and included additional loading from a shroud at the tip of the blade. This shroud is outside the simulated region of the turbine blade. As a result, it is included in the model as an evenly distributed load applied to the surface of the blade section that is furthest from the center of rotation. The magnitude of the force in the distributed load is obtained from a simulation of the whole turbine blade with the baseline geometry. Force balance on the model was achieved by making use of the inertia relief load in Abaqus, which was applied on the surface of the blade section closest to the center of rotation to avoid stress concentrations associated with over constraint of displacements at the boundary of the model. Nonetheless, due to the corners in the model (located at the beginning and end of the extrusion), boundary effects existed in the calculated stress field. As a result, we considered only the stresses from one layer of elements in the extrusion direction, located furthest from boundary effects.

We created an objective function related to the peak stress ratios in the structure to evaluate the performance of different designs.

$$[\phi = \phi_s + p_m + p_Q,] \tag{1}$$

where ϕ is the objective function, ϕ_s is the stress ratio, p_m is the mass penalty, and p_Q is the flux penalty. The stress ratio (ϕ_s) is defined at each integration point in the model as the ratio between the Mises' stress and the temperature dependent yield

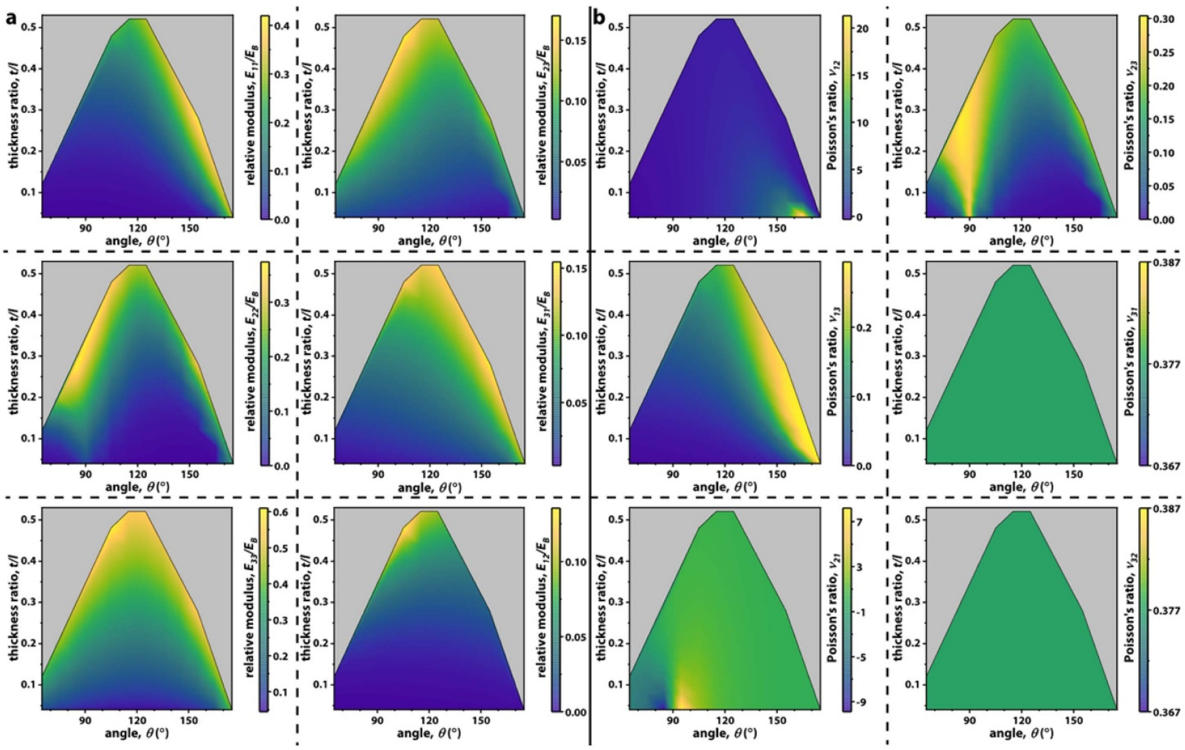

Figure 3. Mechanical characterization of 2.5D generalized honeycomb materials. (a) Elastic and shear moduli at room temperature (when Poisson's ratio of the bulk material is $\nu_B = 0.377$) for the generalized honeycomb materials, normalized by the corresponding bulk properties. (b) Poisson's ratio of the generalized honeycomb materials at room temperature.

stress of the bulk material at that point. The mean of the four highest stress ratios in the model was used to determine the contribution of the stress ratio to the objective function. The additional contributions to the objective function come from penalties that are added to constrain the mass and heat fluxed to the cooling flow of the designs. A mass penalty (p_m) defined as

$$p_m \left\{ \begin{array}{ll} 0 & if mass \leq mass of original design \\ 0.03 + \frac{mass - target\ mass}{target\ mass} & if\ mass > mass\ of\ original\ design \end{array} \right\} \quad (2)$$

was added to designs that had a mass greater than the baseline design. Further, a heat flux penalty (p_Q) given by

$$p_Q = \left\{ \begin{array}{ll} 0 & if flux \leqslant maximum\ allowable flux \\ 0.01 + \frac{flux - target flux}{target flux} & if flux > maximum\ allowable flux \end{array} \right\} \quad (3)$$

was applied to keep the net heat flux from the blade to the cooling flow below the maximum heat that can be removed at the given temperature and flow rate of the cooling air. Note that both penalty functions had a constant term and a proportional term to bias the solution away from the exceeding the mass and flux limits. The magnitude of the constant term was adjusted during small, exploratory optimization runs in order to choose a penalty that was just large enough to ensure that the mass and heat flux constraints would be respected by the optimal solution.

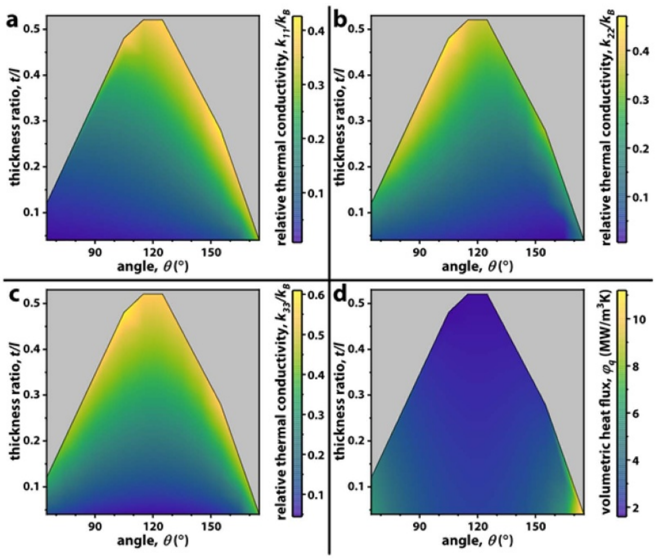

Figure 4. Thermal characterization of the 2.5D generalized honeycomb materials. (a)–(c) The different components of thermal conductivity tensor for generalized honeycomb materials, normalized by the corresponding bulk properties. (d) The maximum volumetric heat flux possible for the different unit cell designs.

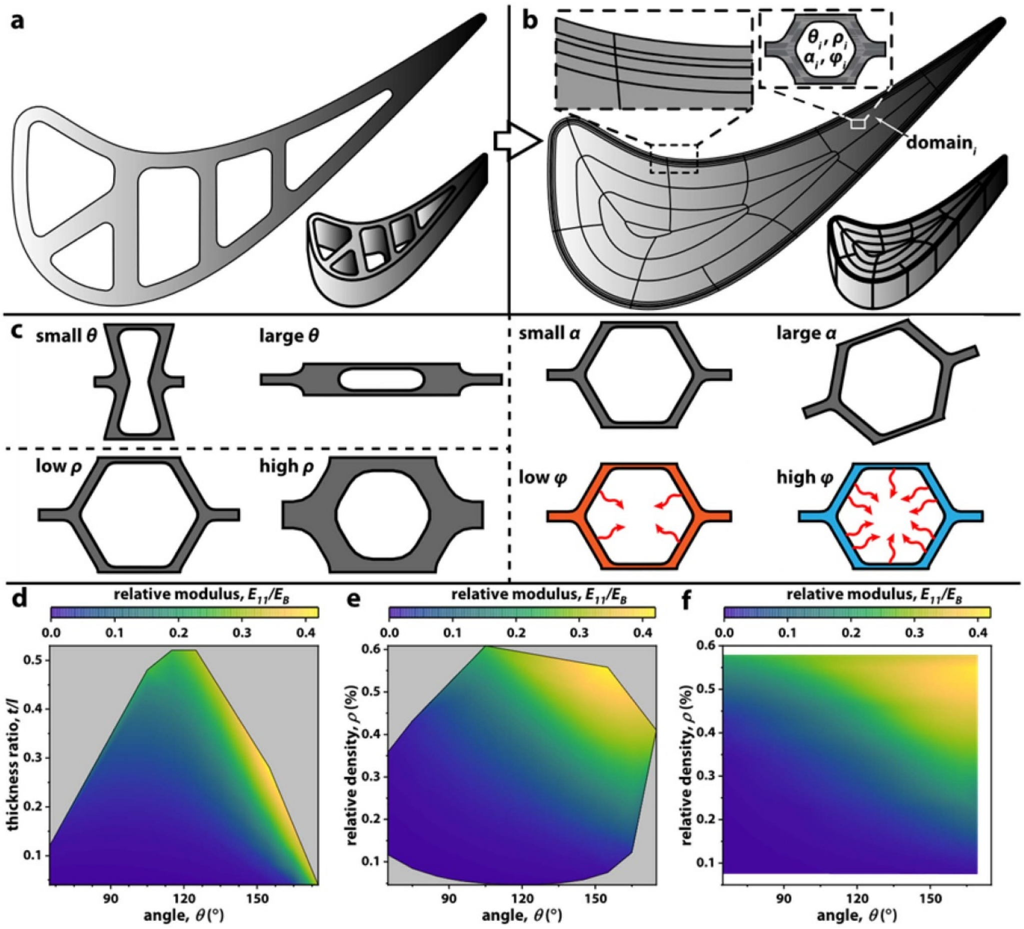

Figure 5. Parameter space remapping and domain generation in the turbine blade section. (a) The cross-section of a traditional turbine blade. (b) The cross-section of our proposed design with architected materials. The section is divided into multiple domains to discretize the material property assignment. (c) Effect of the four optimization variables—honeycomb angle θ, orientation angle α, relative density $\bar{\rho}$, and heat flux fraction φ—on the generalized honeycomb material assigned to each domain. **(d)–(f)** The parameter space is remapped from being defined by (d) thickness ratio *t/l* and angle θ to (e) relative density $\bar{\rho}$ and angle θ, which is further scaled and interpolated to achieve (f) a rectangular parameter space.

4.1. Motivation for meta-function from simulations with random property assignments

In order to gain some insight in the relation between the optimization variables of each domain and the objective function, we performed simulations with randomly assigned variables. The optimization variables are the generalized honeycomb geometric parameters of relative density $\bar{\rho}$ and angle θ, as well as the orientation of unit cells in each domain α, the heat flux φ to the cooling flow from each domain as a fraction of the maximum possible due to its geometry, and the thickness of the solid outer layer *t*. Only the last variable is a global variable, the other four variables are applied independently to each domain, which makes the total number of variables to be $23 \times 4 + 1 = 93$.

From the 25 000 random simulations a clear correlation between the global parameters of outer shell thickness and the heat transferred to the cooling flow from the turbine blade correlate to an improvement of the objective function (figure 6(b)). Following this trend, all future simulations are performed with the thickness of the outer shell layer at its maximum. Due to the cyclic positioning of domains in each layer of the blade and the expectation that sharp changes in material properties across adjacent domains will increase stress—it is expected that domain specific variables that take cyclic values in each layer of domains will produce the lowest objective function values. This trend clearly emerges from the best of the random designs for the relative density $\bar{\rho}$ in the outer layer of domains. Since a similar variation of properties is likely beneficial for the other optimization variables, we utilized this trend to reduce the dimensionality of our optimization function by introducing a meta-function to assign the variables in the domain layers. The meta-function for the honeycomb angle, orientation and flux fraction was defined as a sinusoidal function as following:

$$y_i(n) = x_{i,1} + x_{i,2}\cos\left(\pi\frac{n}{N} + x_{i,3}\right) + lx_{i,4}, \forall i \in [\mathit{honeycomb\ angle},\ \mathit{orientation\ angle}, \mathit{flux fraction}] \quad (4)$$

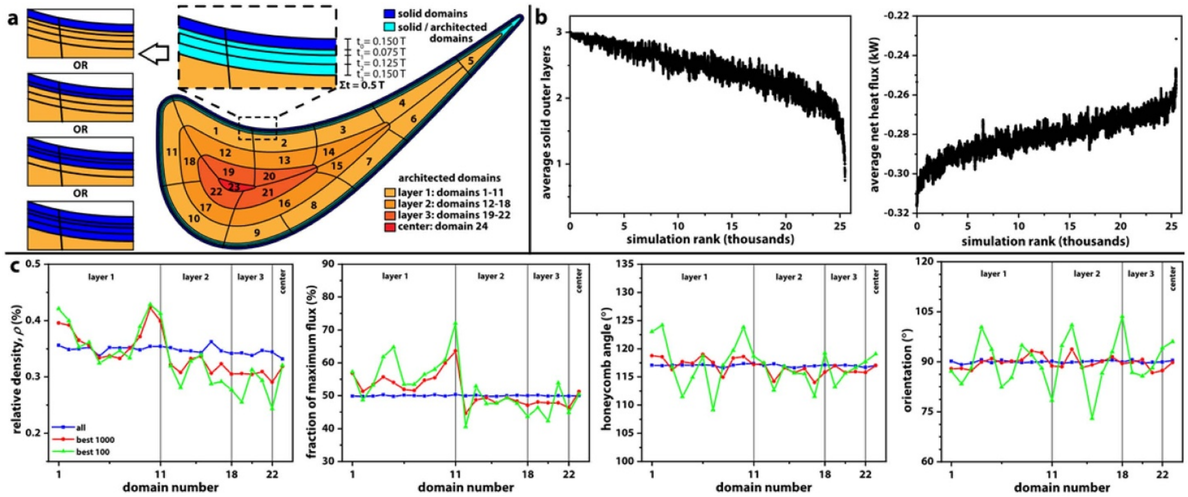

Figure 6. Simulation setup and trends from random parameter assignments. (a) The domains and layers discretized for property assignment. The outermost layer is solid, while the subsequent three layers can be either solid or architected. The thicknesses of the outer layers are provided with respect to the shell thickness T of the baseline design. All numbered domains are architected. (b) Moving average (over 50 simulations) of the number solid outer layers and net heat flux as arranged by simulation rank. The number of solid layers assigned to the model is made discrete [0, 1, 2, or 3] by rounding the value to the nearest integer. The number of solid layers tends toward three, while the magnitude of the heat flux increases with improving simulation rank (simulation rank 1 is the design with the lowest objective function value). (c) Assignment of material properties across domains, as obtained from the best performing random simulations. The observed periodic trend in layer 1 for the relative density $\bar{\rho}$ motivates the meta-function for optimization.

where $y_i(n)$ is the value of variable i in the n^{th} domain in a layer, N is the total number of domains in the layer, l is the layer number (3 for the outermost layer and 0 for the innermost), and $x_{i,j}$ are constants. Since the relative density $\bar{\rho}$ has a strong effect on the effective thermomechanical properties of the generalized honeycomb materials and also appeared to be the dominant parameter in the set of designs with random property assignments, we allowed more freedom to the meta-function for relative density $\bar{\rho}$ by incorporating frequency modulation:

$$y_{relative\,density}(n) = x_1 + x_2 \cos\left[2\pi x_3 \frac{n}{N} + x_4 \sin\left(2\pi x_5 \frac{n}{N}\right) + x_6\right] + l x_7 \tag{5}$$

These meta-functions allowed us to reduce the number of optimization variables to $3 \times 4 + 7 = 19$ while enforcing a cyclical variation of optimization variables in each layer. The enforced sinusoidal assignment of parameter value also ensures a smooth transition in properties among neighboring domains, avoiding stress concentrations at the domain interfaces.

4.2. Optimized design

We used the CMA-ES algorithm in a Python environment (using the *pycma* package [51]) to find the meta-function parameters that minimize the peak stress ratio on the turbine blade. CMA-ES is an optimization algorithm that is well suited for non-linear, non-convex, multi-dimensional functions with many local minima. This gradient free algorithm selects candidate solutions from multivariate normal distributions over the design space. The mean and covariance matrix (which indicates the pairwise dependencies between the variables) of the distribution are updated in each iteration as detailed in [29]. The objective function to be minimized (equation (1)) includes penalties for designs that violate constraints for allowable mass and heat transfer to the cooling flow, since the former cannot be enforced by CMA-ES and the latter is only known after the candidate solution has been evaluated. Given the dimensionality of our optimization function, we used a population size of 90 for each optimization iteration. All of the optimization variables were rescaled and constrained to a [0, 1] range to ensure they have same weights. The arguments passed by the optimization algorithm were used to determine the meta-function value at the centroid for each domain. That meta-function value specified the optimization variables, including the generalized honeycomb geometric design parameters and then assigned the corresponding material properties from our database to each domain of the turbine blade section. With the turbine blade model formed, the mass of the design was calculated and the thermomechanical loading on each design was simulated in Abaqus. The total heat fluxed from the blade along with the fields of Mises' stress and temperature were then extracted from the simulation results and used to calculate the objective function, including any penalties associated with constraint violation.

Figure 7(a) shows the convergence of the objective function value over 200 iterations of the optimization process. The convergence and monotonic reduction of the maximum stress and the stress capacity is shown in figure 7(b). The solid volume of the turbine blade also increases to the maximum amount

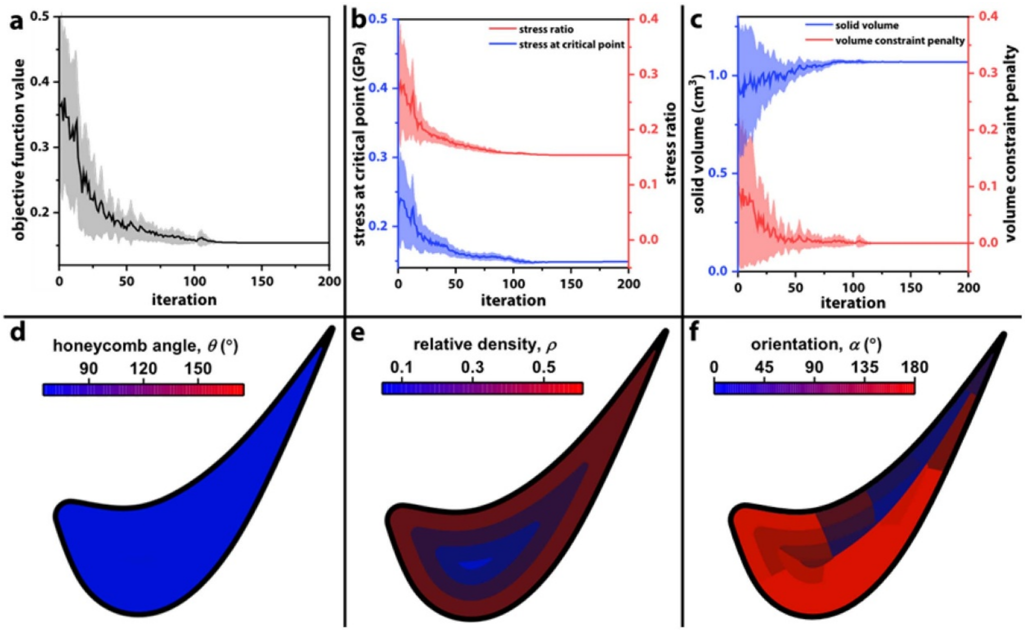

Figure 7. Optimization convergence and results. (a) Convergence of the objective function with increasing iterations. The best objective function value is 0.153, which corresponds to the maximum stress ratio in the optimal solution. (b) The maximum stress and stress ratio both decrease as the optimization progresses. (c) The volume constraint penalty decreases to zero, but the average solid volume increases with increasing iterations. The solid line represents the average value of the parameter over all simulations in an iteration, while the shaded area represents the standard deviation. (d) Distribution of the different design parameters over the turbine blade cross-section.

possible before triggering the mass penalty constraint (p_m) as the optimization converges (figure 7(c)). In all the graphs, the solid line and the shaded area indicate the mean and standard deviation of the variable represented over all the 90 simulations in an iteration.

The optimized variables are shown in figures 7(d)–(f). A clear preference for the honeycomb angle θ across all domains can be seen in figure 7(d), where the minimum possible value of 65° specifies that the most auxetic reentrant honeycomb in our database is best. The auxetic material outperforms more conventional materials by relieving in-plane stresses, which are mostly the product of thermal gradients. Although the optimization reduces the thermal gradient, stress reduction can more effectively be accomplished by reducing the in-plane stiffness of the material. The auxetic generalized honeycomb does just that, without reducing stiffness the direction of extrusion, where it is needed to resist the centrifugal loading.

Figure 7(e) shows that the optimal variation in relative density $\bar{\rho}$ is to be constant within domain layers and reduce across layers of the turbine blade. This makes a radially graded porous structure, with denser outer layers that transition to an almost hollow center. This result can be rationalized by considering the different forces and where they are acting on the turbine blade section: There are two pathways for cooling the interior of a turbine blade: transfer the heat to the cooler portions of the turbine blade by conduction and transfer the heat to the convective cooling flow. Improving these pathways, however, requires different designs of the generalized honeycomb material; more heat transport by conduction comes with higher relative densities, while more heat transport by convection comes with lower relative densities (figure 4). This opposing requirement is taken care of in the optimized solution by assigning the outer layers with a high relative density $\bar{\rho}$ material and the interior with much lower density $\bar{\rho}$. The outer layer, being in contact with the hot fluid, heats up the most; and the high relative density $\bar{\rho}$ of this layer allows efficient conduction to the interior of the turbine blade. Since some convective cooling occurs along the way to the inner layers, not as much conduction is necessary in these layers. Instead, the low relative density $\bar{\rho}$ of the interior allows efficient convective cooling. The denser layers near the exterior also helps to reduce the thermal gradient, which is another driver of stress. Finally, the denser layers near the exterior also increase the second moment of area, which lowers stresses caused by bending moments.

Figures 8(a), (b) show the original and optimized design, each displaying the stress and temperature distribution over the section of the turbine blade body for comparison. It can be seen easily that not only has the maximum stress and temperature decreased for the optimized design, but also their variation is more uniform with less steep gradients. Figures 8(c)–(e) provide a quantitative comparison between the original and optimized design in terms of the most important parameters; the line shows the mean value, the box indicates the $\pm$ 1 standard deviation range and the whiskers show the interquartile range. In the optimized design, the mean Mises' stress is reduced by 42.2%, while the mean temperature above cooling flow shows a 72.1% reduction. The maximum stress also decreases significantly, by 35.4%. Similarly, the maximum temperature also decreases by 17.5%, which means that the temperature of the hot air-fuel mixture around the turbine blade can also be increased by a similar amount. The reduction

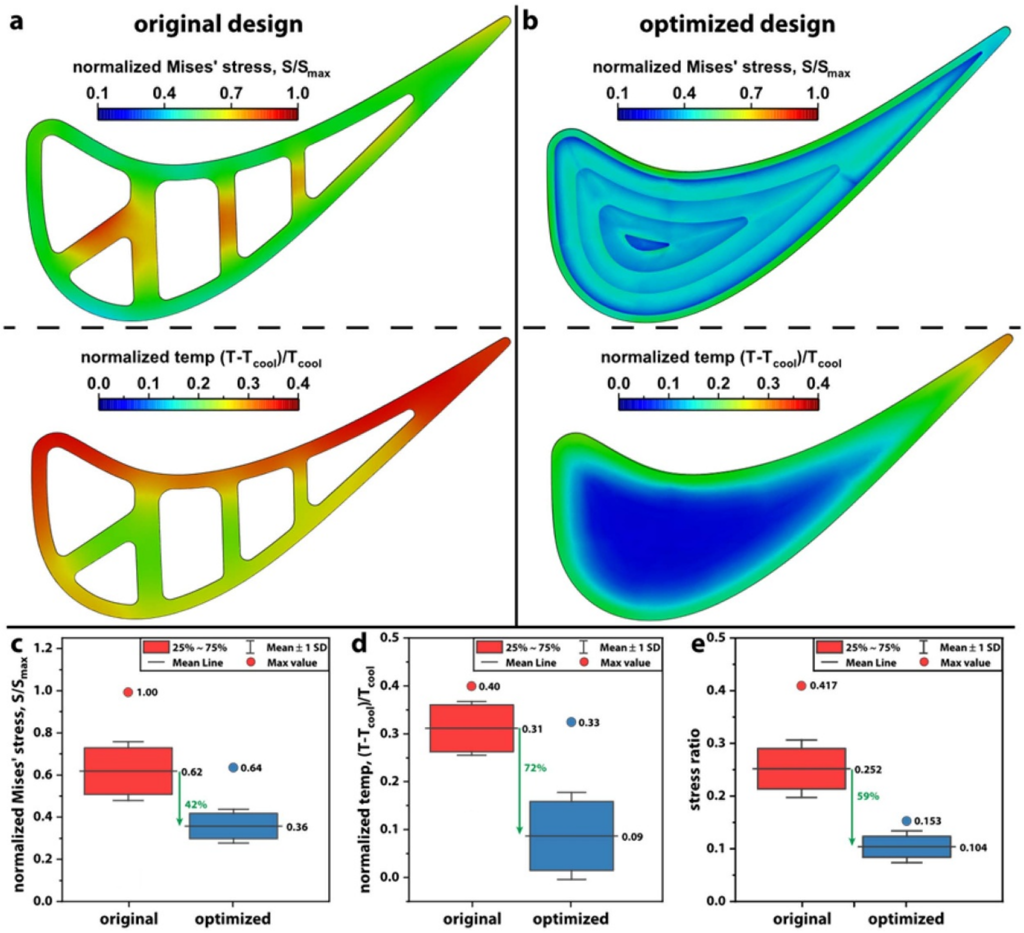

Figure 8. Comparison to and improvement over original design. (a), (b) Results from FE analysis showing the normalized Mises' stress and temperature fields of the (a) original and (b) optimized design during operation. The color bars encompass the range of Mises' stress and temperature over both designs to facilitate comparison. (c)–(e) Comparison of various measures of central tendency and dispersion between the original and optimized design showing the reduction of (c) Mises' stress (normalized by the maximum stress), (d) temperature difference between the blade and the cooling flow (normalized by the temperature of the cooling air flow), and (e) stress ratio. For stress ratio, the mean of the four highest values in the model is indicated as the *max value* as this mean was used to calculate our objective function. All statistics are obtained after mass averaging over the entire model.

in stress and thermal expansion results in smaller deformations during operation, with the mean maximum principal strain reducing by 18.5% (figure S5). While the separate reductions of stress and temperature are beneficial, the objective of the optimization was to minimize the stress ratio, which considers the thermal and mechanical fields together. Minimization of the stress ratio is equivalent to maximizing the factor of safety, which in the optimized design is dramatically increased to 6.54 from 2.41 (171.4% increase) in the baseline design.

5. Conclusion

Here we demonstrated an approach to utilize architected materials to improve the performance of turbine blades. We began by performing a complete thermo-mechanical characterization of 2.5D generalized honeycomb materials by FE simulations followed by optimizing a section of a turbine blade to ascertain the best assignment of local properties to minimize the stress developed during operation. The final design achieved as a result of the optimization process has several advantages over traditional turbine blade designs. First and most importantly, the maximum stress and temperature reached during operation is significantly lower in the optimized design. This indicates that the new design can tolerate hotter turbine inlet temperatures to increase the thermodynamic efficiency of the engine. Second, a much more uniform stress and temperature profile were achieved. Additionally, hollow passages for cool air were replaced by a porous structure, which allowed better dispersion of air throughout the blade and more surface area for heat transfer and led to a significant drop in the average temperature of the blade. Furthermore, this strategy can be used to create a tradeoff between the mass of the blade and the stress developed during operation. Design optimization to achieve minimum mass while maintaining the original stress capacity can be performed to emphasize weight reduction, which can also improve operational efficiencies.

The strategy for using architected materials in turbine blades, at its present level of development, also has three limitations: (i) The homogenized stress within the generalized honeycomb is used, neglecting local stress concentrations. The stress concentrations for generalized honeycomb were found to be large for some stress states (e.g. in plane shear), but local and homogenized stresses are the same for uniaxial stress in the direction of extrusion, which is prevalent in the optimized design. (ii) It does not consider a smooth transition of unit cell design from one domain to another. While the use of a sinusoidal meta-function restricts large changes between two adjacent domains, there are still some stress concentrations at the interface between domains. Moreover, the joining of two adjacent unit cells with different designs is also not considered. (iii) Only static loads and their responses are considered in this study. Gas turbine engines are designed to minimize dynamic loads such as vibration and asymmetric loading, and these effects can be evaluated in a modal analysis to further improve the optimization results. Nevertheless, the results obtained from this study are encouraging and suggest that further investigation will lead to improved turbine blades that can enable more efficient engines.

There is sustained interest in the pursuit of gas turbine engines with greater efficiency. Two of the most actively studied avenues to increase efficiency are the development of new 3D printing technology to additively manufacture turbine blades [52] and the use of ceramic materials for turbine blades [53]. The approach we have taken is compatible with both routes, ensuring that our design is aligned with the future trends of the turbine industry, and presents the opportunity to boost the performance of turbine blades across the spectrum of gas-turbine applications.

Acknowledgments

This work has been funded by Siemens Energy Canada Limited. The authors thank Ali Shanian and Mitch Kibsey (Siemens Energy Canada Limited) for sharing their expertise on turbine blades.

ORCID iD

Andrew J Gross https://orcid.org/0000-0001-7024-1342

References

[1] Bathie W W 1996 *Fundamentals of Gas Turbines* (New York: Wiley)
[2] Yoon W N, Kang M S, Jung N K, Kim J S and Choi B-H 2012 Failure analysis of the defect-induced blade damage of a compressor in the gas turbine of a cogeneration plant *Int. J. Precis. Eng. Manuf.* **13** 717–22
[3] Talya S S, Chattopadhyay A and Rajadas J N 2002 Multidisciplinary design optimization procedure for improved design of a cooled gas turbine blade *Eng. Optim.* **34** 175–94
[4] Wang B, Zhang W, Xie G, Xu Y and Xiao M 2015 Multiconfiguration shape optimization of internal cooling systems of a turbine guide vane based on thermomechanical and conjugate heat transfer analysis *J. Heat Transfer* **137** 061004
[5] Nowak G, Wróblewski W and Nowak I 2012 Convective cooling optimization of a blade for a supercritical steam turbine *Int. J. Heat Mass Transf.* **55** 4511–20
[6] Bolaina C, Teloxa J, Varela C and Sierra F Z 2013 Thermomechanical stress distributions in a gas turbine blade under the effect of cooling flow variations *J. Turbomach.* **135** 064501
[7] Rao V N, Kumar I N N, Madhulata N and Abhijeet A 2014 Mechanical analysis of 1st stage marine gas turbine blade *Int. J. Adv. Sci. Technol.* **68** 57–64
[8] Horlock J H and Torbidoni L 2006 Turbine blade cooling: the blade temperature distribution *Proc. Inst. Mech. Eng. A* **220** 343–53
[9] Rezazadeh Reyhani M, Alizadeh M, Fathi A and Khaledi H 2013 Turbine blade temperature calculation and life estimation - a sensitivity analysis *Propuls. Power Res.* **2** 148–61
[10] Schaedler T A and Carter W B 2016 Architected cellular materials *Annu. Rev. Mater. Res.* **46** 187–210
[11] Silverberg J L, Evans A A, McLeod L, Hayward R C, Hull T, Santangelo C D and Cohen I 2014 Using origami design principles to fold reprogrammable mechanical metamaterials *Science* **345** 647–50
[12] Bückmann T, Thiel M, Kadic M, Schittny R and Wegener M 2014 An elasto-mechanical unfeelability cloak made of pentamode metamaterials *Nat. Commun.* **5** 4130
[13] Coulais C, Teomy E, de Reus K, Shokef Y and van Hecke M 2016 Combinatorial design of textured mechanical metamaterials *Nature* **535** 529–32
[14] Wu J, Aage N, Westermann R and Sigmund O 2018 Infill optimization for additive manufacturing—approaching bone-like porous structures *IEEE Trans. Vis. Comput. Graph.* **24** 1127–40
[15] Evans A G, Hutchinson J W and Ashby M F 1998 Multifunctionality of cellular metal systems *Prog. Mater. Sci.* **43** 171–221
[16] Fleck N A, Deshpande V S and Ashby M F 2010 Micro-architectured materials: past, present and future *Proc. R. Soc. A* **466** 2495–516
[17] Wadley H N G, Fleck N A and Evans A G 2003 Fabrication and structural performance of periodic cellular metal sandwich structures *Compos. Sci. Technol.* **63** 2331–43
[18] Berger J B, Wadley H N G and McMeeking R M 2017 Mechanical metamaterials at the theoretical limit of isotropic elastic stiffness *Nature* **543** 533–7
[19] Schaedler T A, Jacobsen A J and Carter W B 2013 Toward lighter, stiffer materials *Science* **341** 1181–2
[20] Cheng L, Bai J and To A C 2019 Functionally graded lattice structure topology optimization for the design of additive manufactured components with stress constraints *Comput. Methods Appl. Mech. Eng.* **344** 334–59
[21] Wang Y, Zhang L, Daynes S, Zhang H, Feih S and Wang M Y 2018 Design of graded lattice structure with optimized mesostructures for additive manufacturing *Mater. Des.* **142** 114–23
[22] Zhang H, Wang Y and Kang Z 2019 Topology optimization for concurrent design of layer-wise graded lattice materials and structures *Int. J. Eng. Sci.* **138** 26–49
[23] Das S and Sutradhar A 2020 Multi-physics topology optimization of functionally graded controllable porous structures: application to heat dissipating problems *Mater. Des.* **193** 108775
[24] Takezawa A, Zhang X, Kato M and Kitamura M 2019 Method to optimize an additively-manufactured functionally-graded lattice structure for effective liquid cooling *Addit. Manuf.* **28** 285–98
[25] Arabnejad S, Johnston B, Tanzer M and Pasini D 2017 Fully porous 3D printed titanium femoral stem to reduce

stress-shielding following total hip arthroplasty *J. Orthop. Res.* **35** 1774–83

[26] Wang Y, Arabnejad S, Tanzer M and Pasini D 2018 Hip implant design with three-dimensional porous architecture of optimized graded density *J. Mech. Des.* **140** 111406

[27] Aage N, Andreassen E, Lazarov B S and Sigmund O 2017 Giga-voxel computational morphogenesis for structural design *Nature* **550** 84–86

[28] Zhao Z L, Zhou S, Feng X Q and Xie Y M 2018 On the internal architecture of emergent plants *J. Mech. Phys. Solids* **119** 224–39

[29] Blasques J P and Stolpe M 2012 Multi-material topology optimization of laminated composite beam cross sections *Compos. Struct.* **94** 3278–89

[30] Lee Y S, González J A, Lee J H, Kim Y I, Park K C and Han S 2016 Structural topology optimization of the transition piece for an offshore wind turbine with jacket foundation *Renew. Energy* **85** 1214–25

[31] Magerramova L, Vasilyev B and Kinzburskiy V 2016 Novel designs of turbine blades for additive manufacturing *Proc. of the ASME Turbo Expo 2016: Turbomachinery Technical Conf. and Exposition. Volume 5C: Heat Transfer* (American Society of Mechanical Engineers) pp 1–7

[32] Seppälä J and Hupfer A 2014 Topology optimization in structural design of a LP turbine guide vane: potential of additive manufacturing for weight reduction *Volume 7A: Structures and Dynamics* (American Society of Mechanical Engineers) pp 1–10

[33] Martin J H, Yahata B D, Hundley J M, Mayer J A, Schaedler T A and Pollock T M 2017 3D printing of high-strength aluminium alloys *Nature* **549** 365–9

[34] Nandwana P, Elliott A M, Siddel D, Merriman A, Peter W H and Babu S S 2017 Powder bed binder jet 3D printing of Inconel 718: densification, microstructural evolution and challenges *Curr. Opin. Solid State Mater. Sci.* **21** 207–18

[35] Nguyen Q B, Nai M L S, Zhu Z, Sun C-N, Wei J and Zhou W 2017 Characteristics of inconel powders for powder-bed additive manufacturing *Engineering* **3** 695–700

[36] Hansen N, Müller S D and Koumoutsakos P 2003 Reducing the time complexity of the derandomized evolution strategy with covariance matrix adaptation (CMA-ES) *Evol. Comput.* **11** 1–18

[37] Masters I G G and Evans K E E 1996 Models for the elastic deformation of honeycombs *Compos. Struct.* **35** 403–22

[38] Yang L, Harrysson O, West H and Cormier D 2015 Mechanical properties of 3D re-entrant honeycomb auxetic structures realized via additive manufacturing *Int. J. Solids Struct.* **69–70** 475–90

[39] Gibson L J and Ashby M F 1999 *Cellular Solids : Structure and Properties* (Cambridge: Cambridge University Press) https://doi.org/10.1017/CBO9781139878326

[40] Papka S D and Kyriakides S 1998 In-plane crushing of a polycarbonate honeycomb *Int. J. Solids Struct.* **35** 239–67

[41] Park S K and Gao X-L 2008 Micromechanical modeling of honeycomb structures based on a modified couple stress theory *Mech. Adv. Mater. Struct.* **15** 574–93

[42] Abd El-Sayed F K, Jones R and Burgess I W 1979 A theoretical approach to the deformation of honeycomb based composite materials *Composites* **10** 209–14

[43] Ju J and Summers J D 2011 Hyperelastic constitutive modeling of hexagonal honeycombs subjected to in-plane shear loading *J. Eng. Mater. Technol.* **133** 011005

[44] Whitty J P M, Nazare F and Alderson A 2002 Modelling the effects of density variations on the in-plane Poisson's ratios and Young's moduli of periodic conventional and re-entrant honeycombs - Part 1: rib thickness variations *Cell. Polym.* **21** 69–98

[45] Michel J C, Moulinec H and Suquet P 1999 Effective properties of composite materials with periodic microstructure: a computational approach *Comput. Methods Appl. Mech. Eng.* **172** 109–43

[46] Zhang W, Dai G, Wang F, Sun S and Bassir H 2007 Using strain energy-based prediction of effective elastic properties in topology optimization of material microstructures *Acta Mech. Sin.* **23** 77–89

[47] Chung J and Waas A M 1999 Compressive response and failure of circular cell polycarbonate honeycombs under inplane uniaxial stresses *J. Eng. Mater. Technol.* **121** 494

[48] Yang L, Harrysson O, West H and Cormier D 2011 Design and characterization of orthotropic re-entrant auxetic structures made via EBM using Ti6Al4V and pure copper *22nd Annu. Int. Solid Free. Fabr. Symp. - An Addit. Manuf. Conf. SFF 2011* pp 464–74

[49] Qiu C, Guan Z, Jiang S and Li Z 2017 A method of determining effective elastic properties of honeycomb cores based on equal strain energy *Chinese J. Aeronaut.* **30** 766–79

[50] Stronge W J and Shim V P-W 1988 Microdynamics of crushing in cellular solids *J. Eng. Mater. Technol.* **110** 185

[51] Hansen N, Akimoto Y and Baudis P 2019 CMA-ES/pycma on Github

[52] Benzinger A 2017 *Siemens achieves breakthrough with 3D printed gas turbine blades* (Erlangen)

[53] Lu Z, Cao J, Song Z, Li D and Lu B 2019 Research progress of ceramic matrix composite parts based on additive manufacturing technology *Virtual Phys. Prototyp.* **14** 333–48